Persistence of Peregrine Breather in Random Sea States

Jinghua Wang,[1] Q. W. Ma,[1,*] Shiqiang Yan[1] and A. Chabchoub[2]

[1] *School of Mathematics, Computer Science and Engineering, City, University of London, London, EC1V 0HB, United Kingdom*

[2] *Department of Mechanical Engineering, Aalto University, 02150 Espoo, Finland*

Rogue waves are widely recognized as great threats to human oceanic activities. The effectiveness of using the Peregrine breather to model rogue waves has been successfully demonstrated in both numerical and physical wave tank. Additionally, its persistence in random seas has been confirmed in some cases, so that it can also be employed to model rogue waves in random seas. However, based on the results obtained by using the fully nonlinear numerical simulations in this paper, it is reported that the persistence of the Peregrine breather will be affected by the nonlinearities of the random seas, i.e., the spectral bandwidth and the background wave steepness. The investigation on the effects of the two parameters indicates that the Peregrine breather cannot persist thus may not be employed to model rogue waves in random seas in some cases. This paper provides knowledge about how to select background wave parameters, in order to model rogue waves by using the Peregrine breather, which can help saving significant time for designing the experiments.

The rogue waves are defined as waves higher than two times the significant wave height (mean value of the largest one third of the wave heights), and/or crest height higher than 1.2 significant wave height [1]. Modern explanations of rogue waves are reviewed and summarized in [1, 2]. One of the most possible reasons for rogue waves is due to the modulation instability, based on which the 'breather' solutions to the Nonlinear Schrodinger Equation (short as NLSE) are used to model such rogue waves. Early analytical studies on the theory of the breather type solution are well documented and can be found in [3-8].

Generally, a breather may be called a soliton or the superposition of a classical envelope soliton of the NLSE with a plane wave [1]. The Peregrine breather (short as PB) is one of that which admits a large wave localized in both space and time [4]. This feature is very similar with the rogue waves observed in the real ocean, which 'appear from nowhere and disappear without a trace' [9]. Thus, it recently becomes a suitable prototype to be employed to model rogue waves in both laboratory and numerical simulations.

For example, Shemer and Alperovich [10] successfully generated a rogue wave modelled by using PB in a physical wave tank and satisfactory agreement was obtained by comparing the results with that by using numerical simulation based on the NLSE and Dysthe equation. Chabchoub, et al. [11] also reproduced a rogue wave based on the PB in laboratory and found the results agreed very well with the theoretical solution. Later, Chabchoub, et al. [12] successfully simulated a super rogue wave modelled by the PB with amplitude amplified by 5 times of its initial value in a physical wave tank. In addition, Akhmediev, et al. [13] presented the solution describing the spectrum of the PB and pointed out that a triangular spectrum exists at every stage of its development, which suggested the potentially extremely important prospect of identifying spectral signatures of the early emergence of rogue waves resulting from nonlinear wave shaping.

Nevertheless, in reality, the rogue waves are always observed to be accompanied by random background waves (short as RBW). Thus, the effectiveness of the PB for modeling rogue waves in random seas depends on whether it can persist in such situations. More recently, it is confirmed in both laboratory and by weakly nonlinear numerical simulations that the PB is able to persist in random seas [14], which means that the PB can also be adopted for modeling rogue waves in irregular seas. Subsequently, Klein, et al. [15] successfully reproduced the New Year Wave in laboratory by embedding the PB into RBW, and good agreement was achieved.

Despite the fact that the PB can persist in random seas in some cases, one should note that the solution of PB is based on the NLSE, which is an equation up to the third order in wave steepness. That means the PB solution becomes less accurate if it is applied to model large steepness waves. As pointed out by Chabchoub, et al. [12], the measured wave profiles in laboratory can be related well to the theoretical solution only for waves with initial steepness (peak wave number times amplitude) less than 0.06, otherwise the theoretical solution underestimates the maximum crest height measured in laboratory. It implies that stronger nonlinearities due to increasing

wave steepness can affect the persistence of the PB. Heuristically, when the PB is embedded in RBW, the nonlinearities of the superimposed sea, which also depend on the spectral bandwidth and wave steepness of the background waves, can affect the persistence of the PB. It implies that in some cases where the PB cannot persist, the rogue waves in random seas cannot be modelled by using the PB. However, the question whether the persistence of the PB will be affected by the spectral bandwidth and wave steepness of the background waves has not been confirmed so far based on existing literatures. So that, currently, there is no evidence to support that whether the rogue waves in random seas can be successfully generated by using the PB, for a specific the bandwidth and wave steepness. Therefore, we will try to answer this question in this study by carrying out the fully nonlinear numerical simulations. By doing so, the effects of the spectral bandwidth and wave steepness of the background waves on the persistence of the PB will be explored, so that whether the PB can be used for such purpose is justified.

TABLE I Dimensionless variables

Variables	Description
η	Surface elevation multiplied by k_0
$\boldsymbol{X}$	Horizontal space coordinate multiplied by k_0
h	Water depth multiplied by k_0
T	Time variable multiplied by ω_0
ε	Wave amplitude of the uniform part of PB multiplied by k_0
C_g	Wave group speed multiplied by k_0/ω_0
H_s, H_{s0}	Significant wave height of background waves and superimposed waves multiplied by k_0
k_n	Wave number of an individual component multiplied by k_0^{-1}
a_n	Wave amplitude of an individual component multiplied by k_0
ω_n	Wave circular frequency of an individual component multiplied by ω_0^{-1}
L_0	Peak wave length multiplied by k_0
T_0	Peak period multiplied by ω_0
$\phi, \tilde{\phi}$	Velocity potential and that at free surface multiplied by $\sqrt{k_0^3/g}$
$\boldsymbol{K}, K$	Wave number coordinate and its module multiplied by k_0^{-1}
Ω	Wave circular frequency coordinate multiplied by ω_0^{-1}

The fully nonlinear Enhanced Spectral Boundary Integral (short as ESBI) method is employed, which is well documented in [16-20] and details are omitted here. However, the main formulations are briefed for completeness. For convenience, all the variables involved are dimensionless, e.g., the length variables are multiplied by peak wave number k_0, and the time variables by peak circular frequency ω_0, where $\omega_0 = \sqrt{gk_0\tanh(k_0h')}$, g and h' are the gravitational acceleration and water depth, respectively. More specifically, all the dimensionless variables used in this paper are listed in TABLE I. Note that in this study, the peak wave number of the PB is made identical to that of the RBW.

The prognostic equation is given by

$$\frac{\partial \boldsymbol{M}}{\partial T} + \Lambda \boldsymbol{M} + \boldsymbol{P} = \boldsymbol{N} \tag{1}$$

where

$$\boldsymbol{M} = \begin{pmatrix} KF\{\eta\} \\ K\Omega F\{\tilde{\phi}\} \end{pmatrix}, \Lambda = \begin{bmatrix} 0 & -\Omega \\ \Omega & 0 \end{bmatrix}, \boldsymbol{P} = \begin{pmatrix} KF\{v_D\} \\ K\Omega F\{p_G + p_D\} \end{pmatrix}$$

$$\boldsymbol{N} = \begin{pmatrix} K\left(F\{V\} - K\tanh KhF\{\tilde{\phi}\}\right) \\ K\Omega F\left\{\frac{1}{2}\left[\frac{(V+\nabla\eta\cdot\nabla\tilde{\phi})^2}{1+|\nabla\eta|^2} - |\nabla\tilde{\phi}|^2\right]\right\} \end{pmatrix} \tag{2}$$

$\nabla = \partial/\partial \boldsymbol{X} = \partial/\partial X\,\boldsymbol{i} + \partial/\partial Y\,\boldsymbol{j}$ is the horizontal gradient operator, $V = \partial\phi/\partial n\sqrt{1+|\nabla\eta|^2}$ is the vertical velocity, p_G the pressure for the pneumatic wave maker, p_D and v_D the dynamic and mass absorbing term respectively, $\boldsymbol{K} = (\kappa, \lambda)$ is the wave number and $K = |\boldsymbol{K}|$. All the aforementioned variables are non-dimensionlised as shown in TABLE I. The Fourier transform $F\{\}$ and the inverse transform $F^{-1}\{\}$ are defined as

$$\hat{\eta}(\boldsymbol{K}, T) = F\{\eta\} = \int_{-\infty}^{\infty} \eta(\boldsymbol{X}, T)e^{-i\boldsymbol{K}\cdot\boldsymbol{X}}d\boldsymbol{X} \tag{3}$$

$$\eta(\boldsymbol{X}, T) = F^{-1}\{\hat{\eta}\} = \frac{1}{4\pi^2}\int_{-\infty}^{\infty} \hat{\eta}(\boldsymbol{K}, T)e^{i\boldsymbol{K}\cdot\boldsymbol{X}}d\boldsymbol{K} \tag{4}$$

where the Fast Fourier Transform (short as FFT) is adopted to perform the Fourier and inverse transform numerically.

The solution to Eq.(1) is given as

$$\boldsymbol{M}(T) = e^{-\Lambda(T-T_0)}\left[\boldsymbol{M}(T_0) + \int_{T_0}^{T} e^{\Lambda(T-T_0)}(\boldsymbol{N} - \boldsymbol{P})dT\right] \tag{5}$$

where

$$e^{\Lambda\Delta T} = \begin{bmatrix} \cos\Omega\Delta T & -\sin\Omega\Delta T \\ \sin\Omega\Delta T & \cos\Omega\Delta T \end{bmatrix} \tag{6}$$

In addition, the solution to the vertical velocity can be derived with the help of the boundary integral equation, which is given as $V = V_1 + V_2 + V_3 + V_4$ involving the convolution and integration parts. While V_3 and V_4 can be further reformulated as [20]

$$V_3 = \underbrace{V_3^{(1)}}_{4th} + \underbrace{V_3^{(2)}}_{6th} + \underbrace{V_{3,I}}_{integration} \tag{7}$$

$$V_4 = \underbrace{V_4^{(1)}}_{3rd} + \underbrace{V_4^{(2)}}_{5th} + \underbrace{V_4^{(3)}}_{7th} + \underbrace{V_{4,I}}_{integration} \tag{8}$$

and numerical techniques for improving its computational efficiency are proposed in [20], where more details about the ESBI model can be found. Waves can be generated and absorbed by specifying p_G , p_D and v_D in Eq. (2), formulations of which can be found in [18] so are omitted here. The so-called the pneumatic wave maker requires calculating the pressure p_G in Eq. (2) at each time step, which is a function of $\mathbf{X}$ and T decaying exponentially from its centre in space. To do that, one needs the information of frequency, amplitude and phase of each wave component.

To simulate waves incorporating the PB, the analytical expression of the PB is used, which is given by [11], i.e.,

$$A(\xi,\tau) = A_1 + A_2 \qquad (9a)$$

where

$$A_1 = \varepsilon \exp\left(-\frac{i\varepsilon^2}{2}\tau\right) \qquad (9b)$$

is called the carrier wave and is the uniform part, and

$$A_2 = -\varepsilon \exp\left(-\frac{i\varepsilon^2}{2}\tau\right)\left\{\frac{4(1-i\varepsilon^2\tau)}{1+[2\sqrt{2}\varepsilon(\xi-C_g\tau)]^2+\varepsilon^4\tau^2}\right\} \qquad (9c)$$

is a small bulge when ξ and τ are sufficiently large, which can develop into a large wave when both ξ and τ are equal to 0, ε is the wave steepness of the uniform part of the PB, $C_g = 0.5$ is the group speed, $\xi = X - X_f$, $\tau = T - T_f$, X_f and T_f are the specified focusing location and time, respectively. The free surface elevation can be obtained by using

$$\eta_{PB} = Real\{Aexp[i(\xi - \tau)]\} \qquad (10)$$

Meanwhile, one should note that to model rogue waves in random seas for task related simulations, several approaches with specific purposes have been developed. Some studies target at generating rogue waves of specified height and surface slope, e.g., Constrained NewWave [21], some splitting the total energy for the random and focusing part, e.g., method by Kriebel & Alsina [22], while some maintain the spectral shape of the superimposed sea, e.g., method by Wang, et al. [23]. In this study, to embed the PB in random waves while investigating its effects on the persistence of the PB, the spectral shape of the RBW is preserved, thus the following equation is employed

$$\eta = \eta_{PB} + \eta_R \qquad (11)$$

where η_R denotes the RBW,

$$\eta_R = \sum_{n=1}^{N} a_n \cos(k_n X - \omega_n T + \varphi_n) \qquad (12a)$$

the amplitude

$$a_n = \sqrt{2S(\omega_n)\Delta\omega} \qquad (12b)$$

and φ_n is random number distributed in $[0,2\pi)$, k_n and ω_n are the wave number and frequency of the nth component, respectively, N is the total number of the wave components. In this study, we use the JONSWAP spectrum, which is recommended for deep seas by DNV standard [24] and its dimensionless form is given by [25]

$$S(\omega) = \frac{\alpha H_s^2}{\omega^5} exp\left[-\frac{5}{4}\left(\frac{1}{\omega}\right)^4\right]\gamma^{exp[-(\omega-1)^2/(2\varsigma^2)]} \qquad (13)$$

where $\alpha = 0.062(1.094 - 0.019ln\gamma)/[0.23 + 0.0336\gamma - 0.185/(1.9 + \gamma)]$, H_s is the significant wave height representing the background wave steepness, $\gamma \in [1,9]$ is the peak enhancement factor representing the spectral bandwidth, and $\varsigma = 0.07$ if $\omega \le 1$, otherwise $\varsigma = 0.09$. It should be noted that the spectral bandwidth becomes narrower when γ increases.

The method by using Eqs. (12) for generating random waves is called the random phase approach, the limitation of which has been discussed by Tucker, et al. [26], who suggested to use the random amplitude approach. However, according to Elgar, et al. [27], if the total number of spectral component is larger than 1000, no significant difference was found in the statistics produced by using these two approaches. In this study, we cut-off the spectrum at 8 times the peak frequency and let $\Delta\omega = 1/130$, which means a total number of 1040 components are used. It implies random phase approach can be employed in this study, which is equivalent to the random amplitude approach.
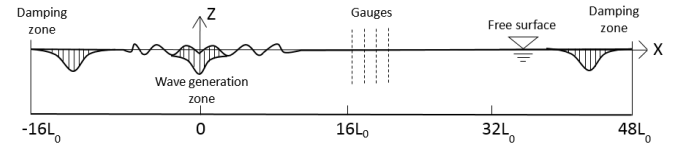

FIG. 1 Configuration of the numerical wave tank

However, it is not straightforward to use Eq.(11) to derive p_G for generating waves in the numerical wave tank. To deal with that, FFT is applied to Eq. (10). Then the resulted information of frequency, amplitude and phase, in addition to that of the RBW in Eq. (11) will be used to formulate p_G in Eq. (2), of which details can be found in [18] and are omitted here.

Before further investigations are carried out, the ESBI method is validated for relevant case. To do that, the simulation of the PB in laboratory [11] is reproduced here numerically, where $k_0 = 11.63m^{-1}$ and other dimensionless variables are $h = 11.63$, $\varepsilon = 0.1047$, $X_f = 11L_0, T_f = 68T_0$. The domain covers 64 peak wave lengths and is resolved into 64 points per peak wave length, which is sufficiently accurate according to [20]. The pneumatic wave maker is placed at $16L_0$ from the left boundary of the tank, where waves are generated and propagated towards both ends, then absorbed in the damping zone to

avoid reflection, as shown in FIG. 1. Note that only the part of the tank of $48L_0$ in length on the right is effectively used for analysis. The free surface elevation at the focusing location obtained by using the ESBI method, in comparison with the laboratory and theoretical results, are shown in FIG. 2(the x-axis is shifted to make $T_f = 0$), where the numerical result agrees very well with the laboratory data and the error of the maximum crest height is only 0.5%, which indicates that the ESBI is very accurate and can be used for the purpose of this study.
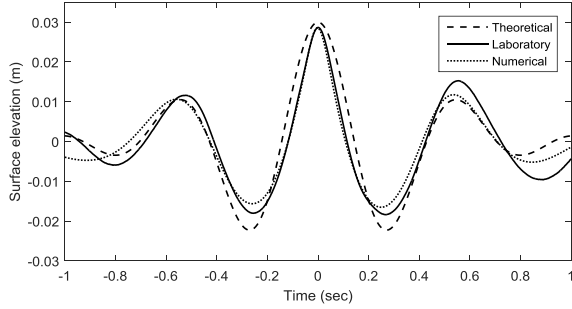

FIG. 2 Free surface elevation of Peregrine breather

TABLE II Choices of parameters

Parameters	Values
H_s/ε	0.333, 0.400, 0.533, 0.573, 0.600, 0.667, 0.733, 0.800, 0.867, 1.000, 1.333, 1.667, 2.000
γ	1, 3, 5, 7, 9

Since the ESBI is validated, the effects of RBW on the persistence of PB in irregular seas can now be explored. The configuration of the numerical wave tanks is the same as that in FIG.1. The duration of the simulation lasts for 130 peak periods, which corresponds to 22 minutes' sea state considering a typical period 10s in the North Sea and is sufficient to achieve the statistical stationary condition [24].

In addition, the range of the parameters involved need to be properly selected, i.e., ε, X_f and T_f in Eq. (9), and H_s and γ in Eq. (13). According to [10], the expected PB amplification factor of 3 renders the initial ε no more than 0.1, otherwise wave breaking occurs, so that we fix the value for $\varepsilon = 0.0873$. Meanwhile, due to the limited tank length, X_f and T_f cannot be arbitrarily large, thus $X_f = 18L_0$ and $T_f = 60T_0$ are chosen in this study. Now, only H_s and γ are adjustable. For the range of γ, several values within 1~9 are selected, which considers most of the cases of the spectral bandwidth in reality [25]. While instead of determining the range of H_s, we use H_s/ε to represent the significance of the RBW steepness against that of the PB. Based on pre-tests, it is found that for $H_s/\varepsilon < 0.333$, the RBW are nearly linear and have neglectable effects on the PB; While for $H_s/\varepsilon > 2$, PB becomes less significant and cannot produce a rogue wave in most of the cases. Based on that, the range of H_s/ε and

γ are summarized in TABLE II, which are then used to perform the fully nonlinear numerical simulations.

As aforementioned, the effectiveness of the PB for modeling the rogue waves in random seas depends on whether it can persist in the background waves. Thus, to associate the PB with rogue waves and quantify the persistence of the PB in random waves, the Abnormality Index is employed for judging whether the rogue waves occur or not due to the PB [12], i.e,

$$I_A = H_{max}/H_{s0} \qquad (14)$$

where H_{max} is the maximum wave height and H_{s0} is the significant wave height of the superimposed sea. Generally, a wave with $I_A \geq 2$ can be identified as rogue wave. Next, the values of I_A in relationship with H_s/ε and γ are investigated through numerical simulations. To obtain the value of I_A, the free surface time history is extracted at the location where the maximum surface elevation appears. For example, the free surface spatial distribution at each grid point is written to files at every time step, which is later used for post-process to find the spatial distribution of the maximum crest height, as shown in FIG. 3 (a). Then the location of the maximum crest height is obtained, i.e., the dash line, at which point the free surface time history is extracted at every time step from the output file, for example as shown in FIG. 3 (b). Next, the up-crossing and down-crossing methods are adopted to estimate the height of each individual wave. Then the maximum wave height H_{max} and the significant wave height H_{s0} can be obtained.

However, based on some pre-tests, it is found that for a case with fixed H_s/ε and γ, the value of I_A changes when using different random phases in Eq.(12a). Thus, before further analysis, the investigation on the effects of random phases are performed. Generally, for a single case with specific H_s/ε and γ, the average and standard deviation of I_A will become stabilized with the increasing number of realizations (each realization is a simulation by using a unique random number sequence as the random phases). To find out how many realizations are required to obtain reliable statistics of I_A, two cases by using $H_s/\varepsilon = 2 \& \gamma = 1$ and $H_s/\varepsilon = 2 \& \gamma = 9$ are simulated, and the errors of the average and standard deviation of I_A are estimated through

$$Err_{avg}(n) = \frac{|avg(I_A)^n - avg(I_A)^{n+1}|}{avg(I_A)^{n+1}} \times 100\% \qquad (15a)$$

$$Err_{std}(n) = \frac{|std(I_A)^n - std(I_A)^{n+1}|}{std(I_A)^{n+1}} \times 100\% \qquad (15b)$$

where $avg(I_A)^n$ and $std(I_A)^n$ denote the average value and standard deviation of I_A based on n realizations, respectively. The results are presented in FIG. 4, which shows that Err_{avg} and Err_{std} drop below 4% after 14 realizations for both the cases, while do not further reduce although number of realizations increases. It indicates

that number of realizations larger than 14 is sufficient to give reliable statistics of I_A, whereas we use 20 in the following analysis. That means for a single case with specific H_s/ε and γ, the simulation is repeated 20 times and each is performed by using a unique random number sequence as the phases. Then I_A is calculated for each realization, which is used for estimate $avg(I_A)$ and $std(I_A)$.

Spatial distribution at T/T_0 = 73.60

(a)

Time history at X/L_0 = 26.69
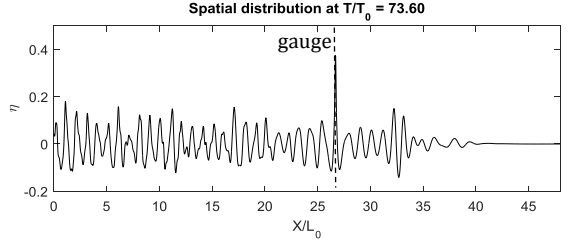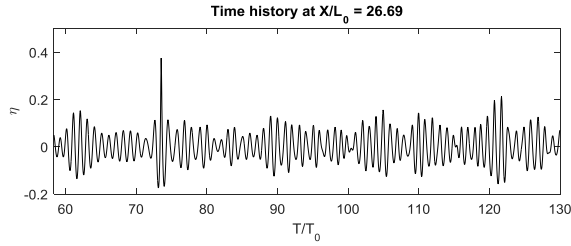
(b)

FIG. 3 Free surface spatial distribution (a) and time history (b) for the case $H_s/\varepsilon = 1.333$ and $\gamma = 1$
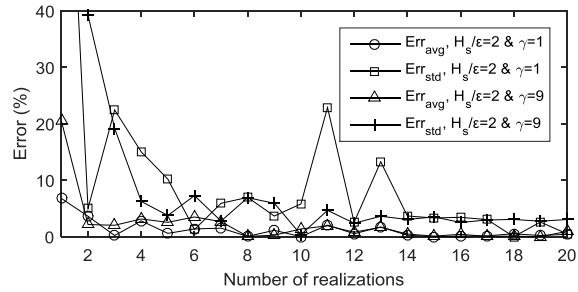
FIG. 4 Err_{avg} and Err_{std} against number of realizations.

By doing so, the values of $avg(I_A) \pm std(I_A)$ are obtained, e.g., that of the case $H_s/\varepsilon = 1$ is shown in FIG. 5. It is found that $avg(I_A)$ increases and the corresponding standard deviation $std(I_A)$ reduces when the spectrum becomes wider (γ decreases). If we now define the lower and upper limits

$$I_A^- = avg(I_A) - std(I_A) \qquad (16a)$$

$$I_A^+ = avg(I_A) + std(I_A) \qquad (16b)$$

then it is understandable that the values of I_A are most likely to be in the range $[I_A^-,\ I_A^+]$. To judge whether the PB can be used to model rogue waves, the minimum value, i.e., I_A^-, needs to be examined. If $I_A^- \geq 2$, it means the whole range $[I_A^-,\ I_A^+] \geq 2$, so that the rogue wave criterion is satisfied and the PB can be employed. Otherwise, partial or the whole range of $[I_A^-,\ I_A^+]$ is less than 2, thus rogue wave criterion cannot always be met so that the PB cannot be used.
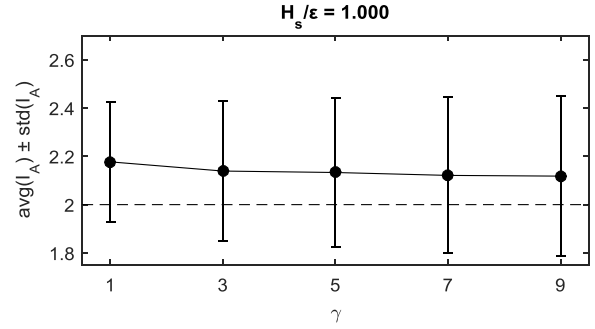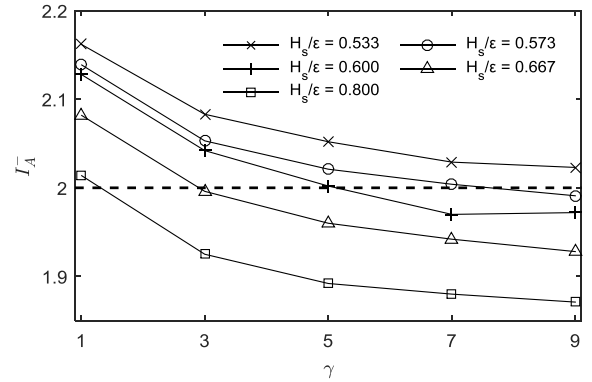
FIG. 5 $avg(I_A) \pm std(I_A)$ against γ

FIG. 6 $avg(I_A)$ against γ and $avg(I_A) - std(I_A)$ against γ
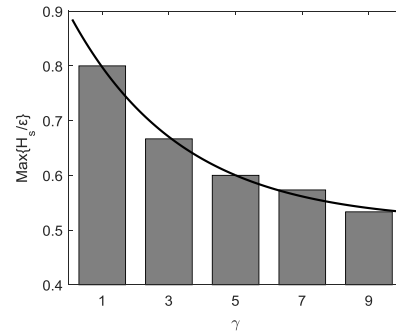
FIG. 7 $Max\{H_s/\varepsilon\}$ against γ

To further illustrate that, values of I_A^- corresponding to some representative cases are shown in FIG. 6, in which it is found that I_A^- increases as the bandwidth becomes larger when H_s/ε is fixed. While it reduces when H_s/ε increases for fixed bandwidth parameter γ. Based on that, the maximum value of H_s/ε is introduced as $Max\{H_s/\varepsilon\}$ for each γ, less than which the rogue wave can be modelled by using the PB. The value of $Max\{H_s/\varepsilon\}$ can be roughly estimated from FIG. 6 by extracting the intersection points between each curve and the line $I_A = 2$. By doing so, the values of $Max\{H_s/\varepsilon\}$ can be obtained in

terms of γ as shown in FIG. 7, where it is seen that the magnitude of $Max\{H_s/\varepsilon\}$ increases as the spectrum becomes wider (γ decreases). Connecting these points gives a curve that divides the area into two zones. It implies that a case with value $H_s/\varepsilon \leq Max\{H_s/\varepsilon\}$ indicates that the PB can persist as $[I_A^-, \ I_A^+] \geq 2$, so that the PB can be employed to model rogue waves in such cases. Otherwise, if $H_s/\varepsilon > Max\{H_s/\varepsilon\}$, then one cannot justify whether PB can persist as the range $[I_A^-, \ I_A^+]$ is partially or wholly less than 2. Therefore, the PB cannot be employed to model the rogue wave in such cases.

In conclusion, the persistence of the Peregrine breather is affected by the spectral bandwidth and the ratio of the steepness of the random background waves over that of the Peregrine breather (H_s/ε). To quantify the persistence of the Peregrine breather and associate that with rogue waves, the Abnormality Index (I_A) for identifying the occurrence of rogue waves is employed. Then numerical simulations are performed and the statistics of I_A are obtained, i.e., the average ($avg(I_A)$) and standard deviation ($std(I_A)$). By examining the lower limit of I_A, i.e. I_A^- in Eq. (16a), the relationship between the maximum ratio $Max\{H_s/\varepsilon\}$ and bandwidth parameter γ is obtained, as shown in FIG. 7, in which it is found that $Max\{H_s/\varepsilon\}$ becomes larger when bandwidth increases. Based on that, one can conclude that, the Peregrine breather can be used for modelling rogue waves in random seas if $H_s/\varepsilon \leq Max\{H_s/\varepsilon\}$; Otherwise one cannot justify whether rogue waves occur so that the Peregrine breather cannot be employed. This study provides a useful reference for designing experiments on modeling the rogue waves or rogue wave-structure interactions, by using the Peregrine breather.

However, this study has fixed focusing time and location and total simulation time, while it has specified a fixed wave steepness of the Peregrine breather and assumes the peak frequency of the random waves is the same with that of the Peregrine breather. Besides, only JONSWAP spectrum is considered in this paper, thus conclusions may change if these conditions are different, and further investigations are needed to explore such effects aforementioned. In addition, the conclusion only applies to two dimensional cases, whereas spreading seas in three dimensional situations will be studied in the future.

*Q.Ma@city.ac.uk

[1] C. Kharif, E. Pelinovsky and A. Slunyaev, Rogue Waves in the Ocean (Springer, New York, 2009).
[2] T. A. A. Adcock and P. H. Taylor, Rep. Prog. Phys., **77**, No. 10, 105901 (2014).
[3] Y. C. Ma, Stud. Appl. Math., **60**, No. 1, 43 (1979).
[4] D. H. Peregrine, J. Aust. Math. Soc. Series B, Appl. Math., **25**, No. 1, 16 (1983).
[5] N. Akhmediev, V. M. Eleonskii and N. E. Kulagin, Theo. Math. Phys., **72**, No. 2, 809 (1987).
[6] K. B. Dysthe and K. Trulsen, Phys. Scr., **T82**, 48 (1999).
[7] A. Calini and C. M. Schober, Phys. Lett. A, **298**, No. 5, 335 (2002).
[8] A. Slunyaev, et al., Physica D, **173**, No. 1, 77 (2002).
[9] N. Akhmediev, A. Ankiewicz and M. Taki, Phys. Lett. A, **373**, No. 6, 675 (2009).
[10] L. Shemer and L. Alperovich, Phys. Fluids, **25**, No. 5, 051701 (2013).
[11] A. Chabchoub, N. P. Hoffmann and N. Akhmediev, Phys. Rev. Lett., **106**, No. 204502, 1 (2011).
[12] A. Chabchoub, et al., Phys. Rev. X, **2**, No. 1, 011015 (2012).
[13] N. Akhmediev, et al., Phys. Lett. A, **375**, No. 3, 541 (2011).
[14] A. Chabchoub, Phys. Rev. Lett., **117**, No. 144103, 1 (2016).
[15] M. Klein, et al., Ocean Eng., **128**, 199 (2016).
[16] D. Clamond and J. Grue, J. Fluid Mech.,**447**, 337 (2001).
[17] D. Fructus, et al., J. Compt. Phys., **205**, 665 (2005).
[18] D. Clamond, et al., J. Compt. Phys., **205**, 686 (2005).
[19] J. Grue, J. Eng. Math., **67**, 55 (2010).
[20] J. Wang and Q. W. Ma, Int. J. Numer. Meth. Eng.,**102**, No.10, 1638 (2015).
[21] P. H. Taylor, P. Jonathan and L. A. Harland, J. Vib. Acoust., **119**, No. 4, 624 (1997)
[22] D. L. Kriebel and M. V. Alsina, in *Proceeding of the 10th International Ocean and Polar Engineering Conference, Seattle, USA, 2000*
[23] J. Wang, S. Yan and Q. W. Ma, CMES-Comp. Model Eng., 106, No. 4, 263 (2015)
[24] DNV, *Environmental conditions and environmental loads* (Det Norske Veritas, Oslo, 2010).
[25] Y. Goda, Coast. Eng. J., **41**, No. 1, 1 (1999).
[26] M. J. Tucker, P. G. Challenor and D. J. T. Carter, Appl. Ocean Res., **6**, No. 2, 118 (1984).
[27] S. Elgar, R. T. Guza and R. J. Seymour, Appl. Ocean Res., **7**, No. 2, 93 (1985)